metals

MDPI

Article

Brittle-Ductile Transition in Laser 3D Printing of Fe-Based Bulk Metallic Glass Composites

Fei Xie [1], Qingjun Chen [1,*] and Jiwen Gao [2]

[1] School of Materials Science and Engineering, Nanchang Hangkong University, Nanchang 330063, China; feixie022718@163.com

[2] School of Civil Engineering, Nanchang Hangkong University, Nanchang 330063, China; 58107@nchu.edu.cn

* Correspondence: qjchen@nchu.edu.cn; Tel.: +86-791-8395-3322

Received: 21 December 2018; Accepted: 10 January 2019; Published: 14 January 2019

Abstract: The effects of the α-Fe phase on mechanical properties and cracking of laser 3D printing Fe-based bulk metallic glass composites were investigated. The elastic recovery and plasticity index were characterized by nanoindentation. As the volume fraction of the α-Fe phase increases from 23.66% to 52.38%, the elastic modulus of printed samples suddenly drops. The samples exhibit a lower deformation resistance, and the plasticity index increases gradually. When the volume fraction of the α-Fe phase is 67.84%, the interaction between the α-Fe phase and matrix phase is smaller during expansion shrinkage. As a result, cracking is easy to initiate, which leads to the highest crack rate of the printed sample. However, as the volume fraction of the α-Fe phase increases to 83.31%, the hard brittle phase was sandwiched between the α-Fe phases similar to the finger structure plays key role in the plastic deformation. The plastic deformation releases large amounts of stress concentrated at the boundary and suppresses crack formation.

Keywords: laser 3D printing; bulk metallic glass; nanoindentation; crack; plasticity

1. Introduction

Fe-based bulk metallic glasses (BMGs) are generally known for their high mechanical strength, excellent corrosion resistance, and wear resistance [1–4]. However, the ambient-temperature brittleness and poor processability strictly limit the scope of their applications [5,6]. To circumvent these limitations, the methods of in situ second ductile phase [7,8] and introducing second phase [9–12] are usually used to improve the plasticity of bulk metallic glass composites.

The additive manufacturing technique, especially laser 3D printing, has been rapidly developed in the past decade [13]. The high scanning speed creates very high cooling rates (10^3–10^8 K/s) [14], higher than the critical cooling rate required for BMGs. However, there are still some problems that hinder its application in the manufacture of BMGs. During the multi-pass scanning of the laser, the deposited layer is subjected to reheating, and amorphous crystallization occurs easily. Thus, it is difficult to obtain fully amorphous structures by laser 3D printing [15]. The rapid heating and cooling during laser 3D printing inevitably induces a large temperature gradient, inducing high thermal stress which creates defects in the 3D printed samples [13]. To alleviate the cracking problem, Lu et al. employed a triple laser scanning strategy in the laser cladding Fe-based BMG process [16]. The results showed that the crystallinity of triple laser scanned samples was higher than that of the single laser scanned samples; however, crack-free samples were obtained. Compared to Fe-based BMGs, the crack-free Zr-based BMGs with high plasticity can be obtained by laser 3D printing, such as $Zr_{52.5}Ti_5Cu_{17.9}Ni_{14.6}Al_{10}$ [17] and $Zr_{55}Cu_{30}Al_{10}Ni_5$ [18]. Since crystallization is unavoidable during laser 3D printing, various phases and different volume fractions can be obtained by adjusting the process parameters. It has been shown

that setting the volume fraction of the α-Fe phase to approximately 40% in Fe-based BMGs composites can improve the plasticity [8].

In this work, α-Fe phases with different volume fractions and morphologies were obtained by different printing parameters, and the effects of the α-Fe phase on mechanical properties and crack initiation and propagation were studied in detail. The aim of this work is to obtain different volume fractions and morphologies of the α-Fe phase by adjusting the printing parameters. Finally, Fe-based BMG composites with high plasticity and fewer cracks can be obtained by laser 3D printing. These would further provide the necessary fundamental basis for obtaining crack-free Fe-based BMG composites with high plasticity using laser 3D printing.

2. Materials and Methods

The $Fe_{41}Co_7Cr_{15}Mo_{14}C_{15}B_6Y_2$ (in at.%) amorphous powders were produced by gas atomization, and the size of powders ranges from 30 μm to 75 μm. Fused deposition modeling (FDM) technology was used in this experiment. The FDM chamber was filled with argon to keep the oxygen level lower than 10 ppm. The focus diameter was 2 mm and each sample printed in two layers. To investigate the influence of the α-Fe phase on the mechanical properties and cracking of laser 3D printed Fe-based BMGs, different printing parameters were used. The details of the power, velocity, and energy density of the samples are listed in Table 1.

Table 1. The process parameters of different samples.

Sample	A	B	C	D	E
Power P (W)	300	300	900	600	900
Velocity v (mm/s)	10	5	10	5	5
Laser energy density LED (J/mm)	30	60	90	120	180

The laser beam energy density LED is critical to the microstructure, surface topography, and properties of the component, and is defined by:

$$LED = \frac{P}{v}, \tag{1}$$

where P is the laser power, and v is the laser scan speed. The usage of a higher laser beam energy density melted more powder, and thicker printed samples were obtained. All of the sample dimensions are summarized in Table 2.

Table 2. The dimensions of different samples.

Sample	A	B	C	D	E
Sample thickness (mm)	0.5	0.8	1	1.2	1.5
Sample width (mm)	10	10	10	10	10
Sample length (mm)	30	30	30	30	30

The phase analyses of the samples were performed using an X-ray diffractometer (XRD) of Bruker D8 type with Cu K_α radiation, and transmission electron microscopy (TEM, FEI TalosF200X, FEI Company, Hillsboro, OR, USA) coupled with energy dispersive spectrometer (EDS). The cross-section of the samples was observed through a Nova NanoSEM 450 field emission scanning electron microscope (FE-SEM, FEI Company, Hillsboro, OR, USA). The crack rate of different samples' cross-sections was calculated using the following equation [19]:

$$R = \sum_{i=1}^{n} \frac{L_i W_i}{LW}, \tag{2}$$

where R is the crack rate, n is the number of the cracks, L_i is the crack length, W_i is the maximum width of a crack, and L and W are the length and width of the sample cross-section.

The mechanical properties of the samples were evaluated by nanoindentation. The tests were performed by an iMicro device from Nanomechanics Inc (Oak Ridge, TN, USA) with a diamond Berkovich, which allowed extracting hardness and elastic modulus directly by using the methodology proposed by Oliver and Pharr [20,21]. The maximum load applied was 50 mN. The reduced elastic modulus E_r is an important parameter for materials of mechanical properties, defined as [22]:

$$\frac{1}{E_r} = \frac{1-v^2}{E} + \frac{1-v_i^2}{E_i}, \tag{3}$$

where v and E are the Poisson's ratio and elastic modulus of the sample, and the diamond indenter with elastic E_i = 1400 GPa and v_i = 0.07. In addition, we also calculated the elastic/plastic indentation energies. The enclosed area between the loading curve and the displacement axis determines the total mechanical work done U_t by the indenter during loading [23]. This energy is defined as the sum of the elastic U_e and plastic U_p energies [22]:

$$U_t = U_e + U_p, \tag{4}$$

The values of U_e were calculated from the area enclosed between the unloading segments and the displacement axis [23]. The elastic recovery U_e/U_t and plasticity index U_p/U_t were obtained as the ratio of the elastic to total energies and the plastic to total energies, respectively, during nanoindentation.

3. Results

3.1. Phase Constitution and Microstructure Characteristics

Figure 1a shows the XRD pattern of the laser 3D printed Fe-based BMG original powder which exhibits only broad diffraction (i.e., fully amorphous structure). The XRD spectra of the laser 3D printed samples (Figure 1b) exhibit sharp crystalline peaks, suggesting that the fabricated samples are crystallized. The crystalline peaks correspond well to α-Fe phase, $Cr_{23}C_6$ phase, and Y_2O_3 phase, respectively. Due to a strong affinity of yttrium towards oxygen, Y_2O_3 forms on the surface of printed samples, corresponding to the intense crystalline peak of Y_2O_3. The right-ward shift of the peaks could possibly be due to the residual stress or defects of the microstructure [24].

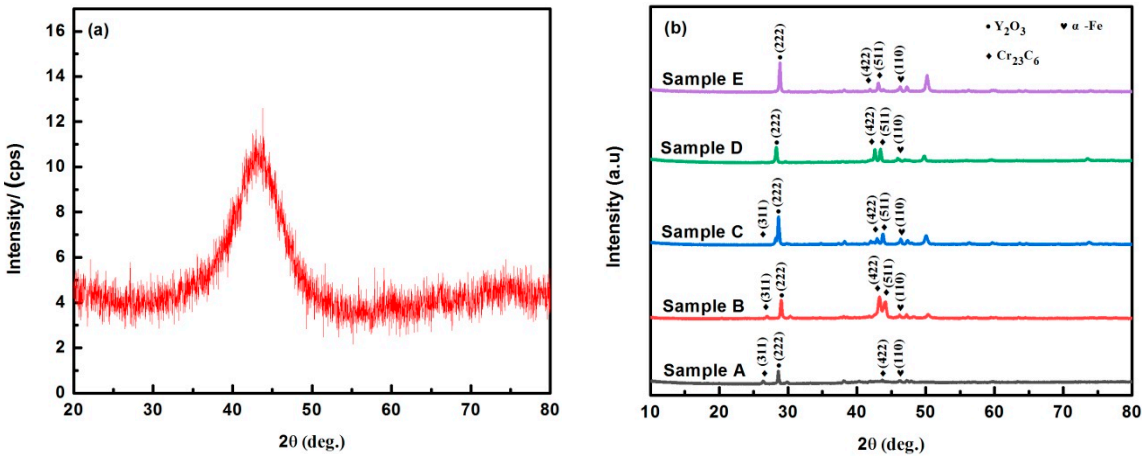

Figure 1. (**a**) X-ray diffraction (XRD) pattern of the Fe-based bulk metallic glass (BMG) powders; (**b**) XRD pattern of samples with different process parameters.

The characteristic cross-section crystalline structures of laser 3D printed samples fabricated using different parameters are shown in Figure 2. It is evident that the cross-sections of printed samples

consist of a raised part and an unraised part. The raised parts are typically cellular, columnar dendrites with extremely fine-grained inter-dendrite spaces. Moreover, the volume fraction of the raised part increases gradually by increasing the laser energy density. This is due to the increase in the laser energy density causing the thickness of printed samples to increase, and the cooling rate inside the sample slowing down, leading to increases in the crystalline phase. From the XRD pattern in Figure 1b, we can also see that the intensity of the crystallization peak increases with increased thickness of the samples.

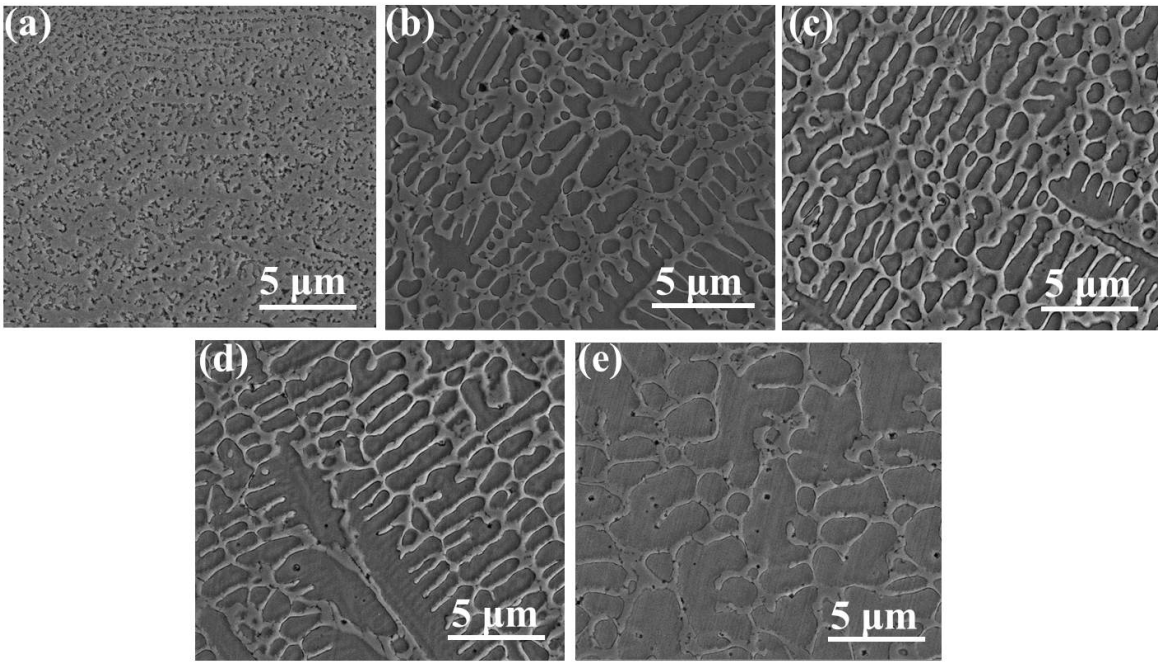

Figure 2. Scanning electron microscope (SEM) images of the microstructures of different printed samples, (**a**) Sample A, (**b**) Sample B, (**c**) Sample C, (**d**) Sample D, and (**e**) Sample E.

A detailed investigation was undertaken by TEM and EDS mapping to gain a better understanding of the phase constitution of the laser 3D printed samples. Three different microstructures and morphologies of printed samples were selected for TEM analysis. Figure 3a shows the high-resolution TEM (HRTEM) micrograph and selected area electron diffraction (SAED) pattern of Sample A. The HRTEM reveals the characteristic amorphous microstructure and lattice fringes. The SAED pattern shows the lattice fringes are α-Fe phase. Figure 3b is the bright field TEM image of Sample D, the microstructure consisting of dendrites and a solid phase in the inter-dendrite spaces. The SAED patterns chosen from the dendrites and solid phase of the inter-dendrite space circled in Figure 3b, indicates that the dendrite (labeled by SA1) is α-Fe phase, and the solid phase of the inter-dendrite space (labeled by SA2) is $Cr_{23}C_6$ phase. It corresponds well with the crystalline phase obtained from XRD patterns. The bright field TEM image and EDS mapping of Sample E are shown in Figure 3c. The SAED indicates that the cellular crystal (labeled by SA3) is α-Fe phase, and the solid phase between cellular crystals is $Cr_{23}C_6$ phase. EDS mapping analysis indicates that the Fe-rich phase is cellular crystals, and the solid phase between cellular crystals is Cr-rich and C-rich, which is consistent with the SAED results.

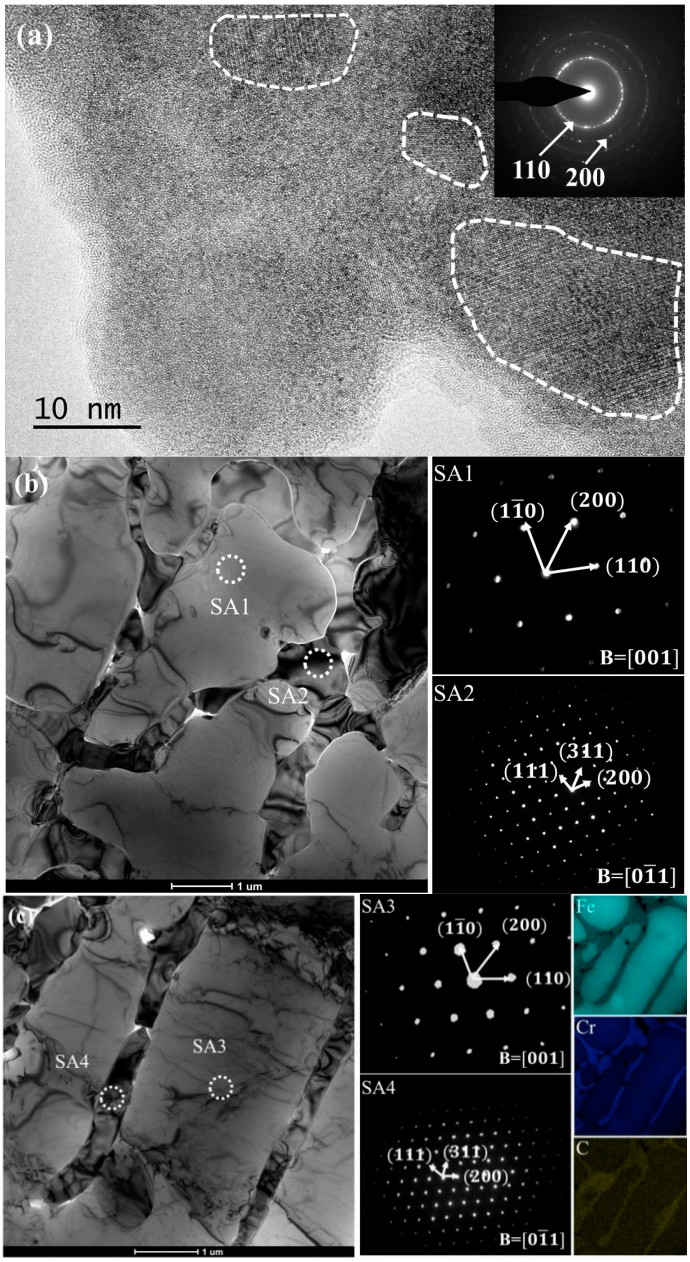

Figure 3. (**a**) High-resolution transmission electron microscopy (HRTEM) micrograph and selected area electron diffraction (SAED) of Sample A; (**b**) TEM image and SAED patterns of Sample D, the SAED patterns of the circled region SA1 and SA2; (**c**) TEM image, SAED patterns and energy dispersive spectrometer (EDS) mapping of Sample E, the SAED patterns of the circled region SA3 and SA4.

3.2. Mechanical Properties

The volume fraction of the α-Fe phase and residual phase (amorphous, $Cr_{23}C_6$, and Y_2O_3 phases) in laser 3D printed samples are calculated by the software Image-Pro Plus. The results are shown in Table 3. Figure 4 shows representative nanoindentation curves of different samples. With the volume fraction of the α-Fe phase increasing, the maximum penetration depth and the final residual indentation depth increase gradually, indicating that the hardness of the samples decreases. The variation in hardness as a function of indentation depth is shown in Figure 5a. The hardness values tended to be stable as the depth reached 350 nm, meaning the hardness was determined from corresponding hardness values with depths greater than 350 nm. Moreover, the curves of elastic modulus-depth

are shown in Figure 5b; when the depth reached 350 nm, the elastic modulus values also tended to be stable.

Table 3. Volume fraction of α-Fe phase in different samples.

Sample	A	B	C	D	E
Volume fraction of α-Fe phase (%)	23.66	52.38	67.84	77.44	83.31
Volume fraction of residual phase (%)	76.34	47.62	32.16	22.56	16.69

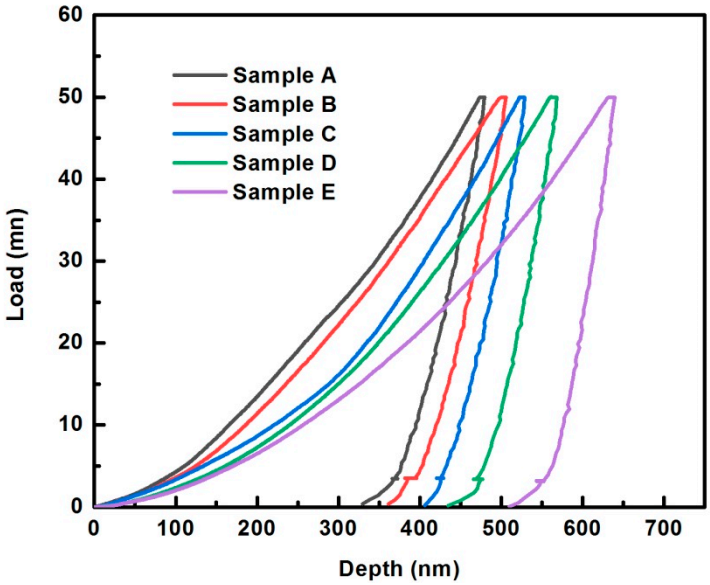

Figure 4. Representative load-depth nanoindentation curves for different printed samples.

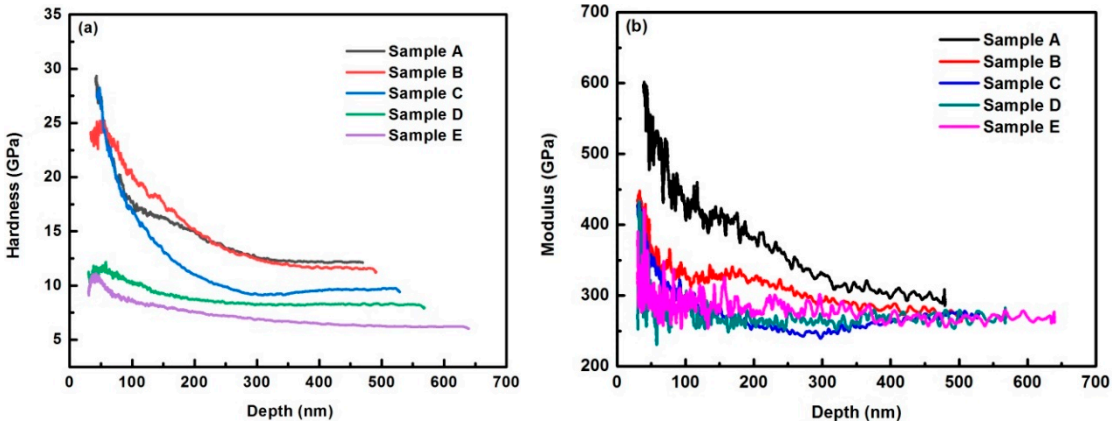

Figure 5. (**a**) The hardness-depth curve of different printed samples; (**b**) The elastic modulus-depth curve of different printed samples.

For each sample, the hardness and elastic modulus have been calculated from an average of 15 indentation depths. As shown in Figure 6, the hardness of Samples A and B change little, staying around 12.5 GPa as the volume fraction of the α-Fe phase increases from 23.66% to 52.38%. Due to the smaller thickness of Samples A and B, the higher hardness can be explained on the basis of substrate confinement effect on the development of the shear bands [25]. However, with an increase in the thickness of the samples, the volume fraction of the crystalline phase increases gradually, and the effect of crystallization on the mechanical properties of the sample becomes more and more prominent. Therefore, the hardness of the samples decreased rapidly, which is mainly related to the crystalline phase of the α-Fe phase [8]. From the Figure 6, the elastic modulus is relatively more sensitive to

the volume fraction of the α-Fe phase and decreases from 301 to 272 GPa. It can be inferred that the sudden drop of elastic modulus may be correlated with the preferred orientation changes from (110) to (200) of the α-Fe phase [26].

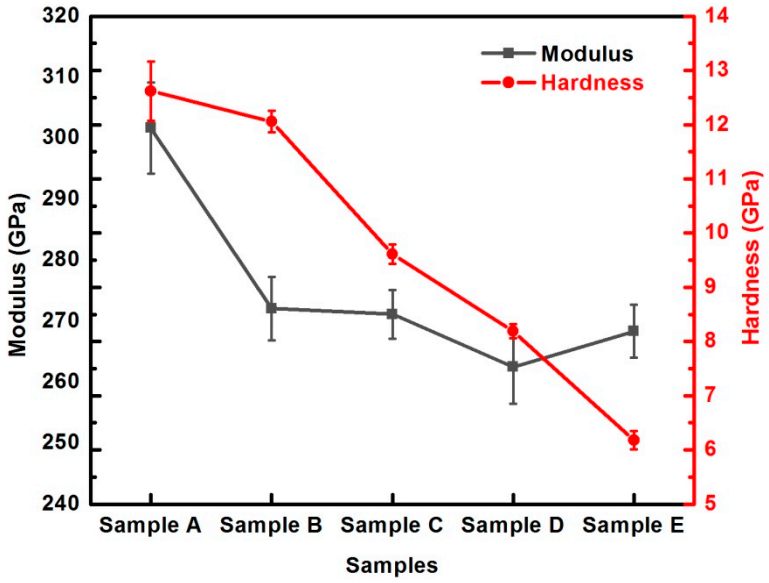

Figure 6. Hardness and elastic modulus of different printed samples.

In addition to hardness and elastic modulus, nanoindentation is also a helpful method to characterize the mechanical properties of the materials [27]. Wear resistance is an important mechanical property of materials, and it is related to the ratio of H/E_r [22]. The higher the ratio of H/E_r, the better the wear resistance of the material [28]. Another parameter related to wear characteristics is H^3/E_r^2, this being indicative of the resistance of the material to plastic deformation when subjected to an applied load contact [29,30]. The higher the value of H^3/E_r^2, the better the material's resistance to plastic deformation [29]. Figure 7a shows the H/E_r and H^3/E_r^2 values of different volume fractions of α-Fe phase. It is clearly seen from the graph that the two aforementioned parameters decrease with increasing α-Fe phase. However, when the volume fraction of the α-Fe phase increases from 23.66% to 52.38%, the values of H/E_r and H^3/E_r^2 fluctuate less, indicating that the α-Fe phase increase from 23.66% to 52.38% has little effect on the wear resistance of the printed samples. This is related to the high hardness of Samples A and B. As the volume fraction of the α-Fe phase reaches 67.84%, the values of H/E_r and H^3/E_r^2 are significantly reduced, which suggests that the plastic deformation resistance of the printed samples decreases.

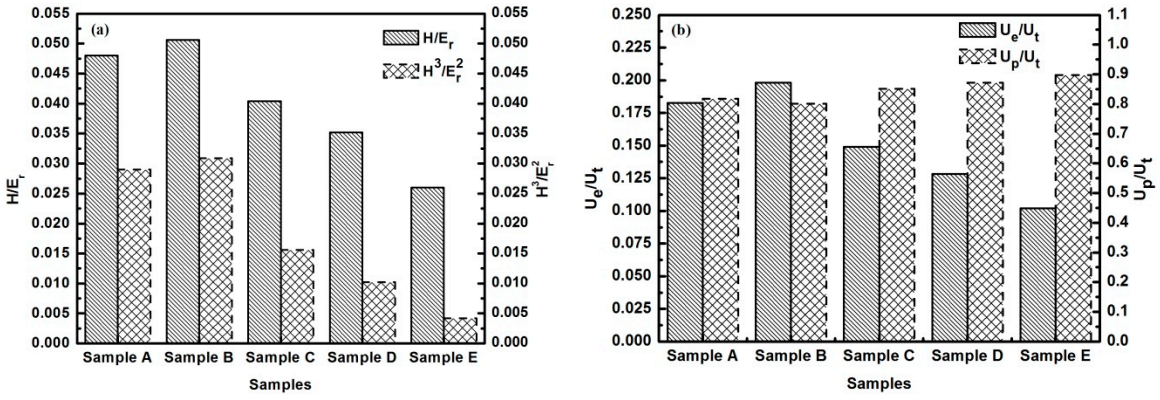

Figure 7. (**a**) The H/E_r and H^3/E_r^2 ratios of different printed samples; (**b**) The elastic recovery U_e/U_t and plasticity index U_p/U_t of different printed samples.

The elastic recovery U_e/U_t and plasticity index U_p/U_t are also important parameters that characterize the mechanical properties of the materials. The elastic recovery U_e/U_t is the energy that is released from the material after being loaded, and it shows the resistance of the material to impact loading [22]. The plasticity index U_p/U_t is related to the intrinsic plasticity of the material [22]. It can be seen from Figure 7b that the plasticity index U_p/U_t increases gradually with increasing α-Fe phase. The values of U_p/U_t with different α-Fe phases are above 0.8, which is close to the $Ti_{40}Zr_{10}Cu_{38}Pd_{12}$ [27] and $Cu_{46.25}Zr_{45.25}Al_{7.5}Er_1$ [31] BMGs, indicating that the printed Fe-based BMGs have intrinsic plasticity thanks to the existence of α-Fe phase.

3.3. Crack Initiation and Propagation

During the laser 3D printing, the melting and solidification of the powders is a complex physical and chemical process, which relates to the formation and transformation of phases and growth morphology of crystal grains [32,33]. The cracks form easily at the hard brittle phase or within inter-dendritic spaces. Figure 8 is a representative SEM image of different volume fraction of the α-Fe phase crack initiation patterns. Figure 8a shows many micro-pores and a straight crack on the sample cross-section. Liu et al. [34] suggests that cracks initiate from the pore and propagate to both sides. Crack propagation along a straight line is shown in Figure 8a. The formation of fine α-Fe phase in Sample A does not affect the propagation of cracks. Figure 8b,d show the crack initiation at two cellular grain boundaries and propagation along the matrix phase. During the laser 3D printing, the dislocations accumulate at the boundary of two α-Fe grains. The stress produced by the dislocation accumulates at the grain boundaries and exceeds the threshold, thereby initiating cracks at the grain boundaries. From Figure 8c we can see crack initiation between dendrites and parallel to the dendrite propagation. The crack stops propagating when it encounters the α-Fe phase marked with red dashed lines shown in Figure 8c,d. This indicates that the α-Fe phase in the crack tip resists the propagation of the crack.

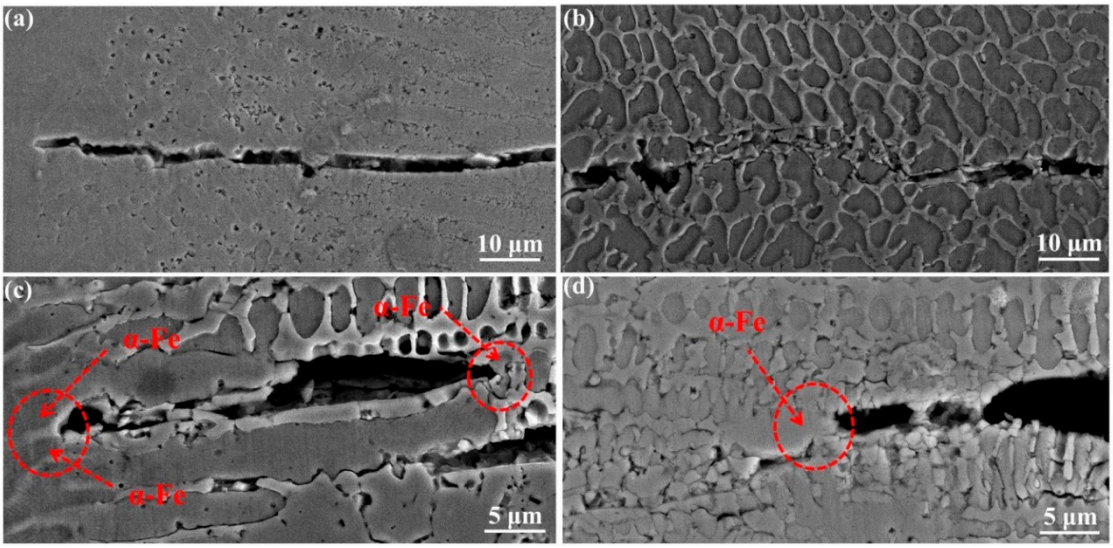

Figure 8. SEM images of crack initiation patterns with different volume fraction of α-Fe phase: (**a**) Sample A, (**b**) Sample B, (**c**) Sample C and (**d**) Sample D.

4. Discussion

The volume fraction and morphology of the α-Fe phase have great influence on crack initiation. Different crack initiation patterns were studied, including crack initiation at the grain boundary of α-Fe grains, and crack initiation between columnar dendrites.

During the laser 3D printing process, dislocations originate from thermal stress, lattice defects, and precipitate in the interior of a crystal [35]. Figure 9a shows dislocations originate from the interior

precipitate of α-Fe crystals. The dislocations in the α-Fe crystals glide and aggregate at the grain boundary under the stress. As shown in Figure 9b, the dislocations accumulate at the boundary of two α-Fe grains (marked with red dashed lines). The stress of the dislocation on a grain boundary is proportional to the number of dislocations. Therefore, the more dislocations accumulating at the grain boundary, the greater the stress. It is shown that the stress concentration of an accumulation group is produced at the grain boundaries of two α-Fe crystals. From the qualitative analysis, it is assumed that the dislocations accumulate sufficiently at the grain boundary. The stress concentration in the accumulation group is very large, and it is possible to initiate a crack at the α-Fe grain boundary. The schematic diagram of crack initiation at a grain boundary is shown in Figure 10. Figure 10a shows that there were a large number of dislocations in the α-Fe phase. Dislocations in the α-Fe crystal glide and aggregate at the grain boundary under the stress. The stress produced by the dislocation accumulation at the two grain boundaries exceeded the threshold, causing the crack to initiate at the grain boundaries, as shown in Figure 10b. The crack propagates along the matrix phase and eventually forms a continuous crack, as presented in Figure 10c.

Figure 8c shows crack initiation between columnar dendrites. The Rappaz-Drezet-Gremaud model [36] suggests that the reduction in pressure between dendrites forms a hole when it reaches the critical pressure point, and leads to initiation of solidification cracks. The inter-dendritic pressure reduction is related to the volume fraction of the solid phase. With more solid phases in the solidified samples, the reflux of inter-dendritic liquid is resisted by the solid phase, so it is easy to initiate cracks between dendrites during solidification shrinkage [37]. In the process of dendrite growth, the root of a dendrite is larger, causing the crack to more easy initiate at the root of the dendrite and propagates along the dendritic growth direction.

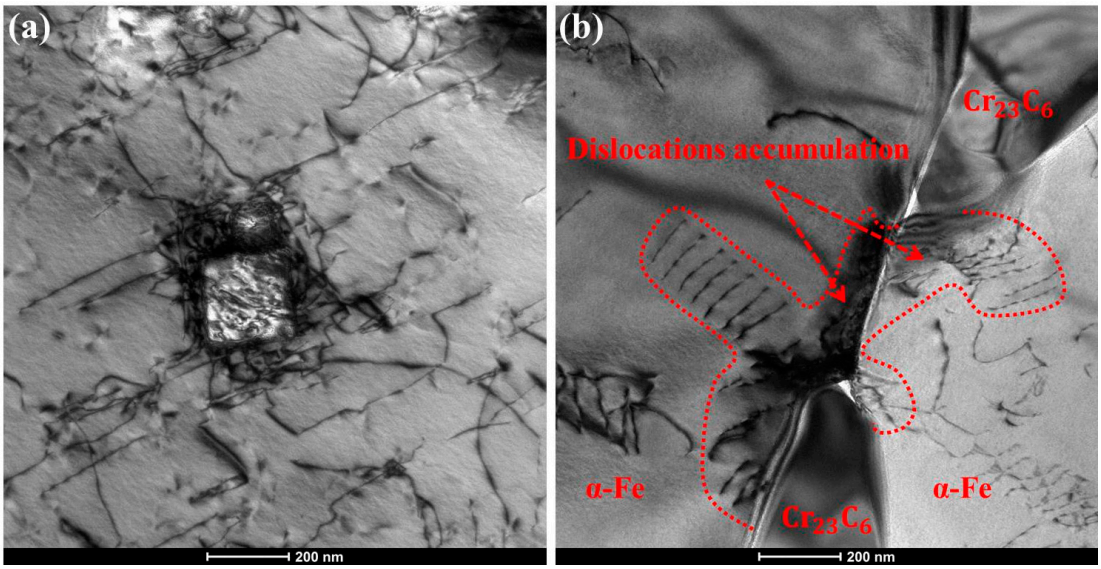

Figure 9. (**a**) Dislocations originate from the interior precipitate of α-Fe crystals; (**b**) The dislocations accumulation at the boundary of two α-Fe phases.

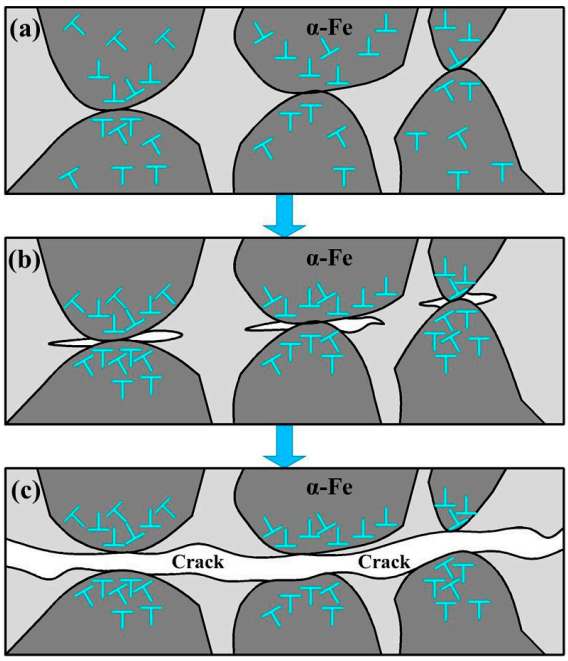

Figure 10. Schematic diagram of the crack initiation mechanism: (**a**) a large number of dislocations in the α-Fe phases; (**b**) dislocations accumulation at the boundary of two α-Fe phases and the initiation of the crack; (**c**) crack propagates along the $Cr_{23}C_6$ phase.

Figure 11 is a fitting function of the volume fraction of the α-Fe phase and the crack rate. It can be known that the relationship between the crack rate and the volume fraction of the α-Fe phase in the samples accord with gauss function, and the fitting equation is: $y = y_0 + \frac{0.18}{11.69\sqrt{\frac{\pi}{2}}} e^{-2\frac{(x-65.88)^2}{136.66}}$. It is clearly seen from Figure 11 that when the volume fraction of the α-Fe phase is lower than 50%, the crack rate is lower and stable at 0.001. The volume fraction of the α-Fe phase decreases while the hard brittle matrix phase increases. During rapid solidification, the hard brittle phase is easily forms micro-cracks, as shown in Figure 8a. However, when the volume fraction of the α-Fe phase is between 50% and 80%, the crack rate is relatively higher. Due to grain boundary stress concentration and the formation of inter-dendritic holes, cracking is easy to initiate at grain boundaries or between dendrites. As the volume fraction of the α-Fe phase increases to 83.31%, crack-free printed samples were obtained.

The brittle-ductile transition during laser 3D printing depends strongly on the structure of α-Fe phase. Both the α-Fe phase and $Cr_{23}C_6$ phase have positive thermal expansion, and the coefficient of thermal expansion of the α-Fe phase is greater than that of the $Cr_{23}C_6$ phase [38,39]. Therefore, the volume change of the α-Fe phase is larger during solidification. When the volume fraction of the α-Fe phase is 67.84%, the crack rate of the printed sample is the highest. It can be inferred that the volume rate of the α-Fe phase to the matrix phase is about 2.2:1; the effect of solidification shrinkage on each is small. Further increasing of the α-Fe phase causes the α-Fe phase and the matrix phase to become wrapped in each other. The shrinkage of the α-Fe phase can be cushioned by the matrix phase. As the volume fraction of the α-Fe phase reaches 83.31%, the hard brittle matrix phase was sandwiched between the α-Fe phases is nearly finger structure, as shown in Figure 3c (the bright field TEM image of Sample E), and causes the deformation of the α-Fe phase during solidification shrinkage. The plastic deformation of the α-Fe phase releases a lot of stress concentrated at the boundary. Stress concentration occurs at the tip of matrix phase, resulting in the formation of dislocations within the grains of α-Fe phase. The dislocation reduces thermal stress by releasing strain energy and thus suppresses crack formation.

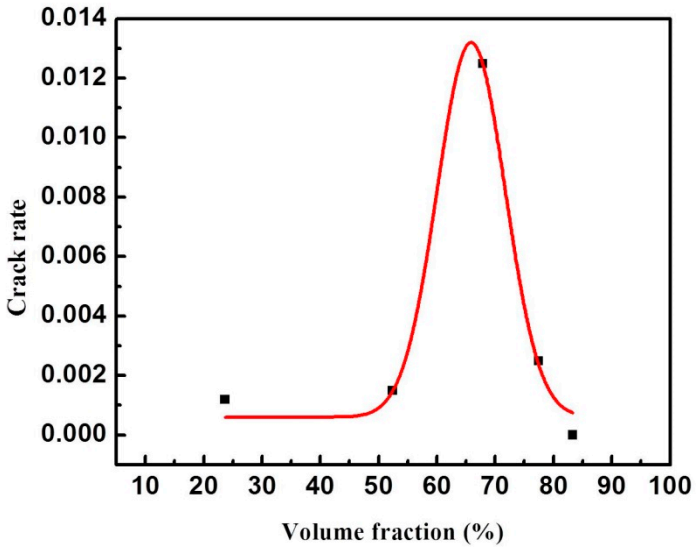

Figure 11. Fitting results of the crack rate with different volume fractions of α-Fe phase.

5. Conclusions

In summary, the different volume fractions of the α-Fe phase were obtained by adjusting the laser 3D printing process parameters. As the volume fraction of the α-Fe phase increases from 23.66% to 52.38%, the hardness of the samples change little. At this point, the hardness is affected by the thickness of the sample. However, when the volume fraction of the α-Fe phase increases to 67.84%, the hardness and wear resistance of the samples decrease rapidly while the plasticity index increases. This is mainly related to the crystalline phase of the α-Fe phase.

The relationship between the crack rate and the volume fraction of the α-Fe phase accords with the distribution of gauss function. When the volume fraction of the α-Fe phase is between 52.38% and 77.44%, it mainly exists in the form of dendrites. Due to the irregular growth of dendrites, a crack is easy to initiate and the crack rate is relatively higher. While the hard brittle matrix phase is wrapped by the α-Fe phase, it causes the deformation of the α-Fe phase. The plastic deformation releases large amounts of stress concentrated at grain boundaries and suppresses crack formation.

Author Contributions: F.X., Q.C., and J.G. conceived and designed the experiment; F.X. and J.G. performed the experiments; all authors analyzed the data and discussed the results; F.X. and Q.C. wrote the paper.

Funding: This work was supported by the National Natural Science Foundation of China (Grant No. 51741105).

Acknowledgments: The authors would like to thank the instrumental analysis center of Nanchang Hangkong University for SEM and TEM assistance, and the Engineering training center of Nanchang University for Nano indentation measurement.

Conflicts of Interest: The authors declare no conflict of interest.

References

1. Su, C.; Chen, Y.; Yu, P.; Song, M.; Chen, W.; Guo, S.F. Linking the thermal characteristics and mechanical properties of Fe-based bulk metallic glasses. *J. Alloys Compd.* **2016**, *663*, 867–871. [CrossRef]
2. Li, Z.; Zhang, C.; Liu, L. Wear behavior and corrosion properties of Fe-based thin film metallic glasses. *J. Alloys Compd.* **2015**, *650*, 127–135. [CrossRef]
3. Zenebe, D.; Yi, S.; Kim, S.S. Sliding friction and wear behavior of Fe-based bulk metallic glass in 3.5% NaCl solution. *J. Mater. Sci.* **2012**, *47*, 1446–1451. [CrossRef]
4. Hou, X.C.; Du, D.; Wang, K.M.; Hong, Y.X.; Chang, B.H. Microstructure and wear resistance of Fe-Cr-Mo-Co-C-B amorphous composite coatings synthesized by laser cladding. *Metals* **2018**, *8*, 622. [CrossRef]

5. Chen, Q.J.; Shen, J.; Zhang, D.L.; Fan, H.B.; Sun, J.F. Mechanical performance and fracture behavior of $Fe_{41}Co_7Cr_{15}Mo_{14}Y_2C_{15}B_6$ bulk metallic glass. *J. Mater. Res.* **2007**, *22*, 358–363. [CrossRef]
6. Guo, S.; Liu, Y. Estimation of critical cooling rates for formation of amorphous alloys from critical sizes. *J. Non-Cryst. Solids* **2012**, *358*, 2753–2758. [CrossRef]
7. Hofmann, D.C.; Suh, J.Y.; Wiest, A.; Duan, G.; Lind, M.L.; Demetriou, M.D.; Johnson, W.L. Designing metallic glass matrix composites with high toughness and tensile ductility. *Nature* **2008**, *451*, 1085–1089. [CrossRef]
8. Guo, S.F.; Liu, L.; Li, N.; Li, Y. Fe-based bulk metallic glass matrix composite with large plasticity. *Scr. Mater.* **2010**, *62*, 329–332. [CrossRef]
9. Liu, L.; Chan, K.C.; Sun, M.; Chen, Q. The effect of the addition of Ta on the structure, crystallization and mechanical properties of Zr–Cu–Ni–Al–Ta bulk metallic glasses. *Mater. Sci. Eng. A* **2007**, *445*, 697–706. [CrossRef]
10. Xu, Y.K.; Ma, H.; Xu, J.; Ma, E. Mg-based bulk metallic glass composites with plasticity and gigapascal strength. *Acta Mater.* **2015**, *53*, 1857–1866. [CrossRef]
11. Li, N.; Zhang, J.; Xing, W.; Ouyang, D.; Liu, L. 3D printing of Fe-based bulk metallic glass composites with combined high strength and fracture toughness. *Mater. Design* **2018**, *143*, 285–296. [CrossRef]
12. Wang, X.; Hu, X.M.; Zhao, L.C.; Jiang, D.X.; Chen, P.; Wang, P.D.; Zhang, Z.P.; Liu, S.Q.; Cui, C.X. Improved plasticity of Ti-based bulk metallic glass at room temperature by electroless thin nickel coating. *Metals* **2017**, *7*, 562. [CrossRef]
13. Gu, D.D.; Meiners, W.; Wissenbach, K.; Poprawe, R. Laser additive manufacturing of metallic components: Materials, processes and mechanisms. *Int. Mater. Rev.* **2013**, *57*, 133–164. [CrossRef]
14. Attar, H.; Bönisch, M.; Calin, M.; Zhang, L.C.; Scudino, S.; Eckert, J. Selective laser melting of in situ titanium–titanium boride composites: Processing, microstructure and mechanical properties. *Acta Mater.* **2014**, *76*, 13–22. [CrossRef]
15. Zhang, Y.; Lin, X.; Wang, L.; Wei, L.; Liu, F.; Huang, W. Microstructural analysis of $Zr_{55}Cu_{30}Al_{10}Ni_5$, bulk metallic glasses by laser surface remelting and laser solid forming. *Intermetallics* **2015**, *66*, 22–30. [CrossRef]
16. Lu, Y.Z.; Huang, G.K.; Wang, Y.Z.; Li, H.G.; Qin, Z.X.; Lu, X. Crack-free Fe-based amorphous coating synthesized by laser cladding. *Mater. Lett.* **2018**, *210*, 46–50. [CrossRef]
17. Li, X.P.; Roberts, M.P.; O'Keeffe, S.; Sercombe, T.B. Selective laser melting of Zr-based bulk metallic glasses: Processing, microstructure and mechanical properties. *Mater. Design* **2016**, *112*, 217–226. [CrossRef]
18. Ouyang, D.; Li, N.; Xing, W.; Zhang, J.J.; Liu, L. 3D printing of crack-free high strength Zr-based bulk metallic glass composite by selective laser melting. *Intermetallics* **2017**, *90*, 128–134. [CrossRef]
19. Zhang, J.; Singer, R.F. Hot tearing of nickel-based superalloys during directional solidification. *Acta Mater.* **2002**, *50*, 1869–1879. [CrossRef]
20. Oliver, W.C.; Pharr, G.M. An improved technique for determining hardness and elastic modulus using load and displacement sensing indentation experiments. *J. Mater. Res.* **1992**, *7*, 1564–1583. [CrossRef]
21. Oliver, W.C.; Pharr, G.M. Measurement of hardness and elastic modulus by instrumented indentation: Advances in understanding and refinements to methodology. *J. Mater. Res.* **2004**, *19*, 3–20. [CrossRef]
22. Hynowska, A.; Pellicer, E.; Fornell, J.; González, S.; Steenberge, N.V.; Suriñach, S.; Gebert, A.; Calin, M.; Eckert, J.; Baró, M.D.; et al. Nanostructured β-phase Ti–31.0Fe–9.0Sn and sub-μm structured Ti–39.3Nb–13.3Zr–10.7Ta alloys for biomedical applications: Microstructure benefits on the mechanical and corrosion performances. *Mater. Sci. Eng. C* **2012**, *32*, 2418–2425. [CrossRef]
23. Bao, Y.W.; Wang, W.; Zhou, Y.C. Investigation of the relationship between elastic modulus and hardness based on depth-sensing indentation measurements. *Acta Mater.* **2004**, *52*, 5397–5404. [CrossRef]
24. Bakshi, S.D.; Sinha, D.; Chowdhury, S.G. Anisotropic broadening of XRD peaks of, α′-Fe: Williamson-Hall and Warren-Averbach analysis using full width at half maximum (FWHM) and integral breadth (IB). *Mater. Charact.* **2018**, *142*, 144–153. [CrossRef]
25. Ghidelli, M.; Gravier, S.; Blandin, J.J.; Djemia, P.; Mompiou, F.; Abadias, G.; Raskin, J.P.; Pardoen, T. Extrinsic mechanical size effects in thin ZrNi metallic glass films. *Acta Mater.* **2015**, *90*, 232–241. [CrossRef]
26. Song, J.M.; Wang, D.S.; Yeh, C.H.; Lu, W.C.; Tsou, Y.S.; Lin, S.C. Texture and temperature dependence on the mechanical characteristics of copper electrodeposits. *Mater. Sci. Eng. A* **2013**, *559*, 655–664. [CrossRef]
27. Fornell, J.; Steenberge, N.V.; Varea, A.; Rossinyol, E.; Pellicer, E.; Suriñach, S.; Baró, M.D.; Sort, J. Enhanced mechanical properties and in vitro corrosion behavior of amorphous and devitrified $Ti_{40}Zr_{10}Cu_{38}Pd_{12}$ metallic glass. *J. Mech. Behav. Biomed. Mater.* **2011**, *4*, 1709–1717. [CrossRef] [PubMed]

28. Medeiros, B.B.; Medeiros, M.M.; Fornell, J.; Sort, J.; Baró, M.D.; Jorge, A.M. Nanoindentation response of Cu–Ti based metallic glasses: Comparison between as-cast, relaxed and devitrified states. *J. Non-Cryst. Solids* **2015**, *425*, 103–109. [CrossRef]
29. Musil, J.; Kunc, F.; Zeman, H.; Poláková, H. Relationships between hardness, Young's modulus and elastic recovery in hard nanocomposite coatings. *Surf. Coat. Technol.* **2002**, *154*, 304–313. [CrossRef]
30. Hynowska, A.; Blanquer, A.; Pellicer, E.; Fornell, J.; Suriñach, S.; Baró, M.D.; González, S.; Ibáñez, E.; Barrios, L.; Nogués, C.; et al. Novel Ti-Zr-Hf-Fe Nanostructured Alloy for Biomedical Applications. *Materials* **2013**, *6*, 4930–4945. [CrossRef]
31. Yang, F.; Li, D.; Yang, M.X.; Li, R.; Jiang, W.H.; Wang, G.Y.; Zhang, T.; Liaw, P. Localized deformation of a $Cu_{46.25}Zr_{45.25}A_{l7.5}Er_1$ bulk metallic glass. *J. Phys. D Appl. Phys.* **2009**, *42*, 065401. [CrossRef]
32. Kurz, W.; Giovanola, B.; Trivedi, R. Theory of Microstructural Development During Rapid Solidification. *Acta Metall.* **1986**, *34*, 823–830. [CrossRef]
33. Rohatgi, P.K.; Asthana, R.; Das, S. Solidification, structures, and properties of cast metal-ceramic particle composites. *Metall. Rev.* **2013**, *31*, 115–139. [CrossRef]
34. Liu, H.; Yang, S.; Xie, C.; Zhang, Q.; Cao, Y. Mechanisms of fatigue crack initiation and propagation in 6005A CMT welded joint. *J. Alloys Compd.* **2018**, *741*, 188–196. [CrossRef]
35. Klapper, H. Generation and propagation of dislocations during crystal growth. *Mater. Chem. Phys.* **2000**, *66*, 101–109. [CrossRef]
36. Rappaz, M.; Drezet, J.M.; Gremaud, M. A new hot-tearing criterion. *Metall. Mater. Trans. A* **1999**, *30*, 449–455. [CrossRef]
37. Griffith, A.A. The Phenomena of Rupture and Flow in Solids. *Philos. Trans. R. Soc. Lond.* **1921**, *221*, 163–198. [CrossRef]
38. Wang, J.W.; Gong, Y.Y.; Liu, J.; Miao, X.F.; Xu, G.Z.; Chen, F.H.; Zhang, Q.M.; Xu, F. Balancing negative and positive thermal expansion effect in dual-phase La(Fe,Si) 13/α-Fe in-situ composite with improved compressive strength. *J. Alloys Compd.* **2018**, *769*, 233–238. [CrossRef]
39. Quadakkers, W.J.; Piron-Abellan, J.; Shemet, V.; Singheiser, L. Metallic interconnectors for solid oxide fuel cells a review. *High Temp. Technol.* **2003**, *20*, 115–127. [CrossRef]